Supporting Information for: Spin-State Selective Excitation in Spin Defects of Hexagonal Boron Nitride

Mohammad Abdullah Sadi,[*,†,‡] Luca Basso,[¶] David A Fehr,[§] Xingyu Gao,[‡] Sumukh Vaidya,[‡] Emmeline G Riendeau,[¶,∥] Gajadhar Joshi,[¶] Tongcang Li,[‡,†,⊥,#] Michael E Flatté,[§] Andrew M Mounce,[*,¶] and Yong P Chen[*,‡,†,⊥,#]

†*Elmore Family School of Electrical and Computer Engineering, Purdue University, West Lafayette, Indiana 47907, USA*

‡*Department of Physics and Astronomy, Purdue University, West Lafayette, Indiana 47907, USA*

¶*Center for Integrated Nanotechnologies, Sandia National Laboratories, Albuquerque, New Mexico 87123, USA*

§*Department of Physics and Astronomy, University of Iowa, Iowa City, Iowa 52242, USA*

∥*Department of Physics, University of Chicago, Chicago, Illinois 60637, USA*

⊥*Birck Nanotechnology Center, Purdue University, West Lafayette, Indiana 47907, USA*

#*Purdue Quantum Science and Engineering Institute, Purdue University, West Lafayette, Indiana 47907, USA*

E-mail: msadi@purdue.edu; amounce@sandia.gov; yongchen@purdue.edu

Experimental setup

Sample Preparation

Commercial hBN flakes (2D Semiconductors) were exfoliated onto a silicon substrate and irradiated with 2.5 keV He+ ions at a fluence of 0.2 nm^{-2} using an ISIS3000 ion implanter (PSP Vacuum Technology) to generate (V_B^-) defects. The irradiated hBN flakes were then transferred onto a gold waveguide using a polycarbonate (PC) stamp mounted on a polydimethylsiloxane (PDMS) block. The transfer process involved heating the substrate to 160 °C, cooling to 50 °C, and lifting the PC stamp with the hBN flakes. The stamp was then brought into contact with the gold substrate, heated to 190 °C to melt the PC film, and the PDMS was removed. The substrate was cleaned with chloroform, acetone, and isopropanol to ensure clean deposition of the hBN flakes.

Waveguide Fabrication

The gold on sapphire cross-shaped waveguide was fabricated using photolithographic patterning with an MLA 150 Maskless Aligner, followed by gold deposition using a metal evaporator. The printed circuit board (PCB) for connecting the waveguide was fabricated using an LPKF Protolaser U4.

Optical and microwave signal generation and processing

The optical configuration for capturing the ODMR signal (Fig. S1) consists of a green laser of 532 nm for sample illumination, and longpass filter for red light detection coupled to a single photon counter (SPCM) for V_B^- hBN experiments. Microwave signal generation and transmission are performed by the FPGA ZCU111 in combination with the Quantum Instrument Control Kit - Defect Arbitrary Waveform Generator (QICK-DAWG), with microwave amplification provided by a dedicated microwave amplifier. Data collection and processing are also handled by the FPGA system. QICK-DAWG,[1] an open-source software package developed at Sandia National Laboratories, enables laser control, microwave pulsing, and low-frequency readout for NV control and measurement. The package is adopted and modified to be suitable for V_B^- hBN experiments. A translation stage with a fixed permanent magnet is employed for the V_B^- hBN experiments.

CW ODMR is performed by continually driving microwaves and laser illumination while detecting the number of emitted photons through a SPCM to a function counter (Keysight 53320A). Photon counts were typically accumulated for 1ms per microwave frequency data point. At each frequency point we also collected a background signal with microwave off to account for any drift in PL intensity. We then sweep across the microwave frequency range, with this entire frequency sweep then repeated multiple times to improve signal-to-noise ratio through averaging.

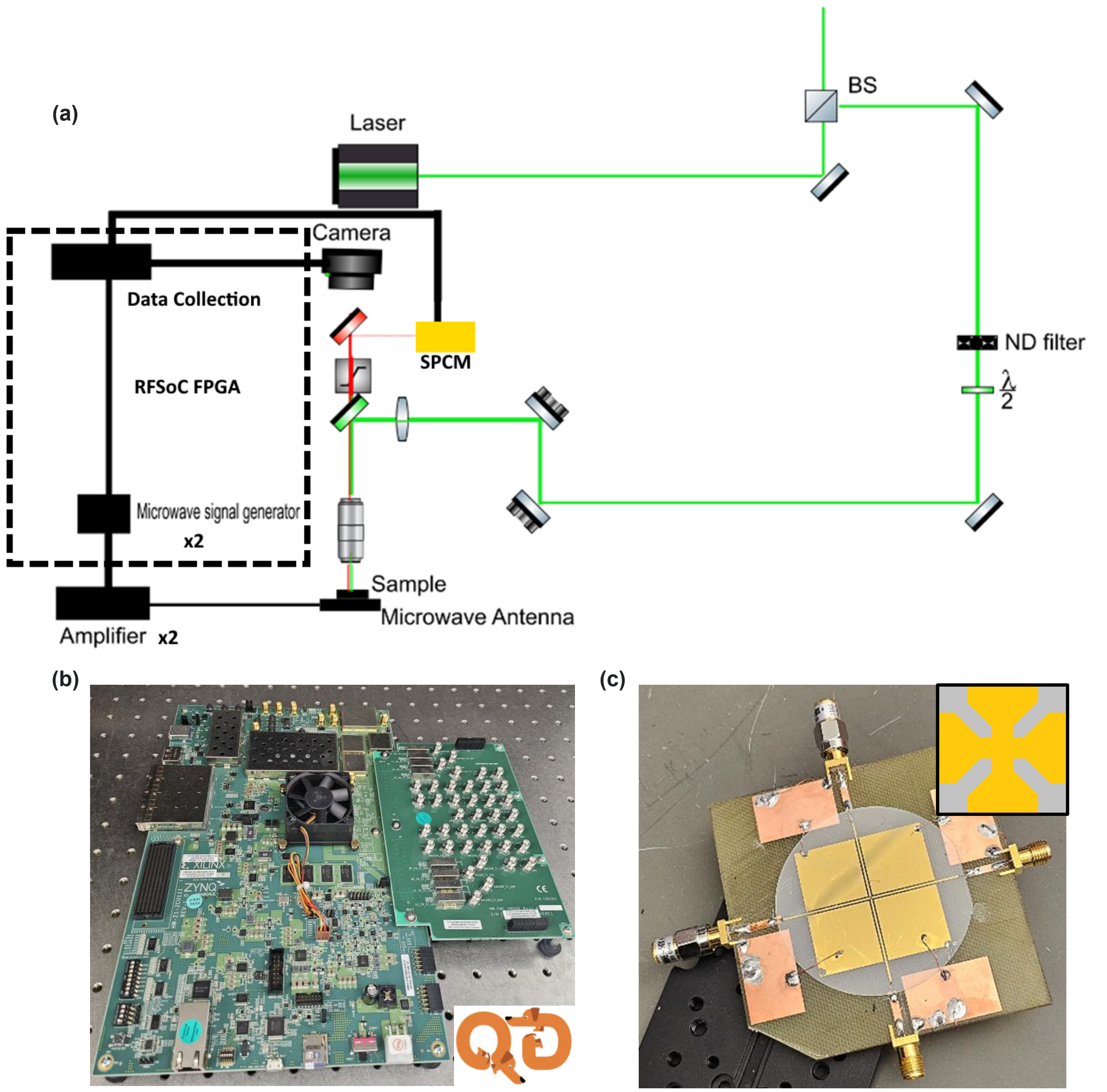

Figure S1: Experimental setup for phase-synced dual microwave excitation of V_B^- defects in hBN. (a) Schematic diagram of the experimental apparatus, including optical components, microwave generation and delivery systems, and data processing units. (b) ZCU111 RFSoC FPGA controlled using the Qick-Dawg package for synchronized microwave generation, precise timing control, and real-time data processing. (c) Gold cross-waveguide is deposited on sapphire substrate, with 50 Ω terminations at the ends of orthogonal microwave transmission lines. Rectangular gold pads serve as ground planes. The inset shows that the waveguide narrows to a 50 μm width at the center to enhance B_{MW} delivery. The device is mounted on a laser-etched copper printed circuit board.

Lindblad Model Implementation

Lindblad calculations were completed with a 7-level model and similar optical rates as Whitefield et al.[2] In the notation of Whitefield et al.,[2] we used $k_p = 7\ \mu s^{-1}$, $k_d = 880\ \mu s^{-1}$, $k_{45} = 1.15\ ns^{-1}$, $k_{35} = 220\ \mu s^{-1}$, $k_{52} = 20\ \mu s^{-1}$, and $k_{51} = 13\ \mu s^{-1}$. In adapting the model and rates from Whitefield et al.[2] to the 7-level model used in this work, we assumed the following correspondence: $\langle 4|\hat{\rho}|4\rangle \simeq \langle e|\langle +1|\hat{\rho}|+1\rangle|e\rangle + \langle e|\langle -1|\hat{\rho}|-1\rangle|e\rangle$ and $\langle 2|\hat{\rho}|2\rangle \simeq \langle g|\langle +1|\hat{\rho}|+1\rangle|g\rangle + \langle g|\langle -1|\hat{\rho}|-1\rangle|g\rangle$. In other words, the population in state $|4\rangle$ is equivalent to the total population in states $|e\rangle|\pm 1\rangle$, and the population in state $|2\rangle$ is equivalent to the total population in states $|g\rangle|\pm 1\rangle$. Finally, we adjusted k_{35} from its value in Whitefield et al.[2] to allow the calculated Contrast to match the measured Contrast in this work.

Magnetic sensitivity analysis of circularly polarized spin-state excitation in V_B^- hBN

Circularly polarized microwave-driven spin-selective excitation provides clearly resolved spectral features. The magnetic sensitivity for CW ODMR[3] is quantified as:

$$\eta_B = A \times \frac{h}{g\mu_B} \times \frac{\Delta\nu}{C\sqrt{R}} \tag{1}$$

where η_B is the magnetic field sensitivity (precision), A is a numerical factor related to the lineshape ($A \approx 0.77$ for Lorentzian profiles), h is the Planck constant, g is the Landé g-factor, μ_B is the Bohr magneton, $\Delta\nu$ is the ODMR linewidth (FWHM), C is the ODMR contrast, and R is the photon count rate.

Using data obtained with circularly polarized microwave excitation at 2.31 mT magnetic field, double Lorentzian fitting (Figure S2) yields a linewidth of $\Delta\nu = 224.1$ MHz and contrast of $C = 6.61\%$ for the primary peak ($|0\rangle$ to $|\text{-}1\rangle$ transition). With a photon count rate of $R = 4.525 \times 10^6$ Hz, this results in a magnetic sensitivity of $\eta_B = 44\ \mu\text{T}/\sqrt{\text{Hz}}$.

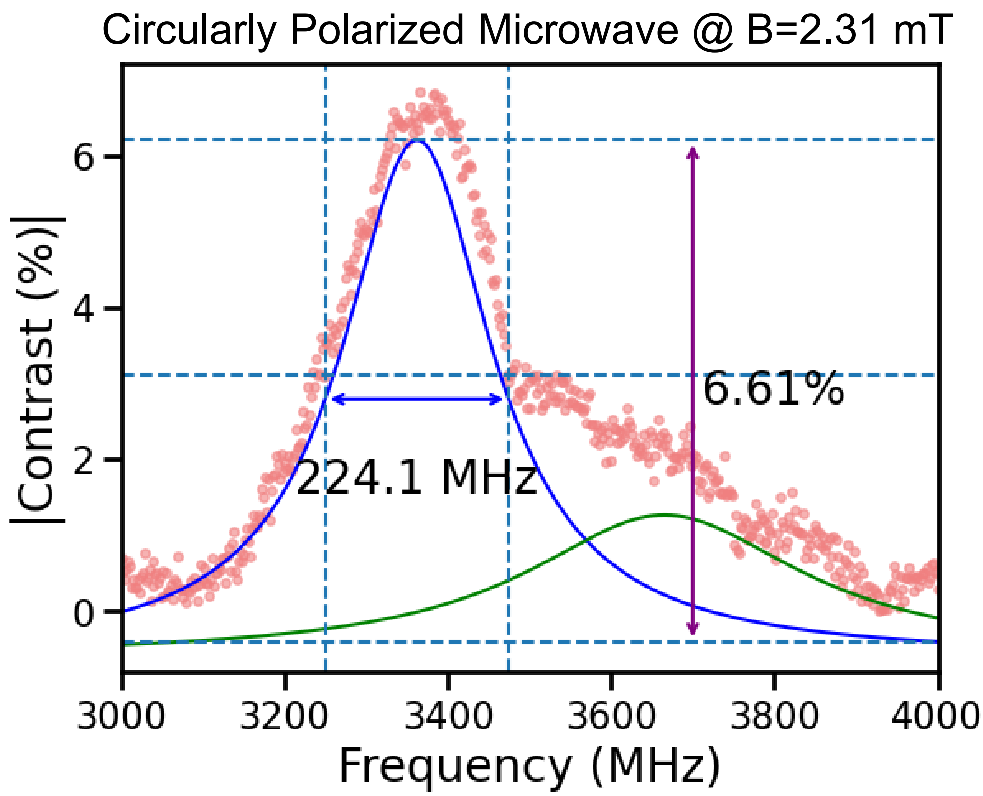

Figure S2: ODMR spectrum at 2.31 mT magnetic field fitted with double Lorentzian functions for circularly polarized microwave excitation with maximum selective excitation of the $|0\rangle$ to $|\text{-}1\rangle$ transition. Raw data points (light coral) are fitted with double Lorentzian functions (blue and green curves). FWHM and contrast values are indicated for the primary peak.

Our measured contrast of 6.61% and sensitivity of 44 $\mu T/\sqrt{Hz}$ are within reasonable agreement with literature values for V_B^- defects. Since its initial demonstration with modest ODMR contrast of ∼0.6%,[4] significant advances in V_B^- performance have been achieved through various approaches including excited-state ODMR spectroscopy,[5–7] plasmonic enhancement reaching contrasts up to 46%,[8] photonic engineering,[9] and systematic optimization of sensing protocols.[2] Our microwave circular polarization technique specifically targets the challenging low and zero magnetic field regimes where conventional approaches are fundamentally limited by spectral overlap. This enables entirely new sensing paradigms such as zero-field magnetometry and cross relaxometry that are not accessible with traditional ODMR approaches.

Magnetic field-dependent deviations in microwave phase difference between spin-state selective transitions in V_B^- hBN

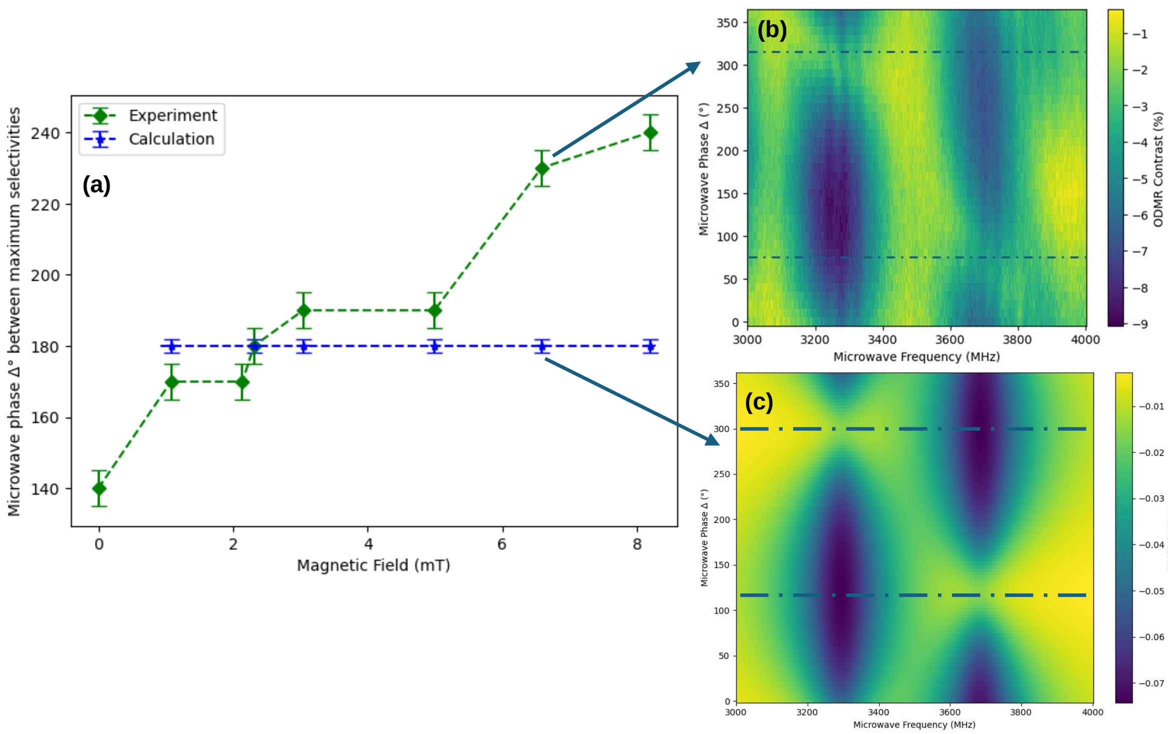

Figure S3: Magnetic field dependence of phase separation between maximum spin-state selectivities. (a) Relationship between observed phase differences ($\Delta°$) of orthogonal linearly polarized microwaves for maximum spin-state selectivities and the applied magnetic field into the device, showing experimental data (green) with error bars from microwave phase step size and theoretical calculations (blue) that fail to capture the observed deviations from 180° at field extremes. (b) Color plot of experimental ODMR spectra evolution versus phase difference ($\Delta°$) at 6.58 mT into the device, with blue dashed lines marking maximum selectivity conditions. (c) Corresponding Lindblad calculations at 6.58 mT showing 180° phase separation between maximum selectivity conditions, differing from experimental data in (b).

Our measurements reveal unexpected variations in the phase differences between the two Δs each corresponding to maximum selectivity for the two spin-state transitions individually. These show significant deviations from the expected 180° separation predicted by Equation 3 in the main manuscript. For magnetic field pointing into the device, this 180°

separation appears to hold approximately true only within a limited magnetic field range of 2-5 mT. At zero field, we observe a smaller phase separation of only 140°, while at higher fields reaching 8.2 mT, the separation increases significantly to 240°. The error bars shown in our experimental measurements reflect the microwave phase step size used during the scanning process. The comparison between experimental ODMR spectra evolution and theoretical predictions at 6.58 mT highlights this discrepancy. While experimental data shows variable phase separation between maximum selectivity conditions marked by blue dashed lines, the corresponding Lindblad calculations show a constant phase separation that differs from experimental observations. In case of zero magnetic field, there is negligible change in selectivities of the two separate spin-state transitions with microwave phase change during calculation, with both transitions equally favored, so Δ can be stated as undefined.

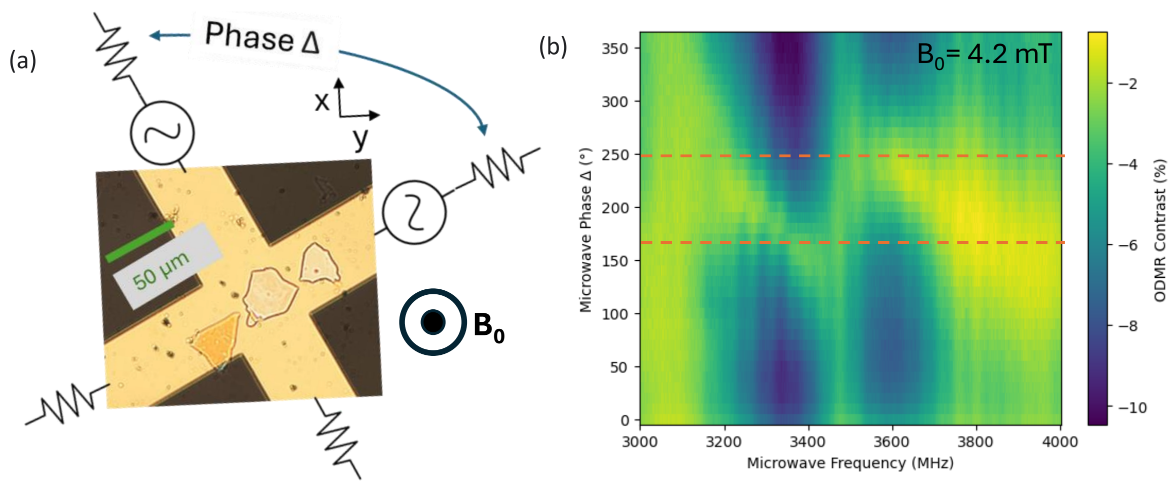

Figure S4: Inverted magnetic field orientation affecting spin-state selectivity in V_B^- defects in hBN. (a) Experimental configuration with the magnetic field oriented coming out of the plane, in contrast to the going into-the-plane orientation described in the main manuscript. (b) Spin-state selectivity under this reversed field configuration, demonstrating around 90° phase difference (Δ°) separation between maximum selectivities (indicated by dashed oranged lines), as opposed to the approximately 180° separation observed in the main manuscript for the into-the-plane field orientation for the same magnetic field strength.

In our investigation of an inverted magnetic field configuration with the field oriented coming out of the plane, we observe maximum spin-state selectivities in V_B^- hBN separated by a microwave phase difference (Δ) of around 90°, which contrasts with the approximately

180° separation observed for similar strength into-the-plane fields. These observed deviations in both standard and inverted field configurations might potentially be related to similar underlying factors. Changes in the effective angle between the defect symmetry axis and the microwave magnetic field B_{MW} could play a role, as this angle may not remain perpendicular at all field strengths or orientations. This misalignment might result in the projection of supposedly circular microwave polarization in the x-y plane onto the defect axis as elliptical and vice versa. Our theoretical calculations do not capture these observed deviations, suggesting additional factors may be involved that are not accounted for in our current models. Various additional factors could include stray fields, distortions of defects, or device-induced alterations to the plane where B_{MW} is rotating, though these have not been fully characterized in this study. Our observations suggest that there may be a complex interplay between applied magnetic field, microwave polarization, and the atomic structure of V_B^- defects in hBN. Further investigation into these phenomena could yield insights for improving device performance and understanding of the defects.

References

(1) Riendeau, E. G.; Basso, L.; Mah, J. J.; Cong, R.; Sadi, M.; Henshaw, J.; Azizur-Rahman, K.; Jones, A.; Joshi, G.; Lilly, M. P.; Mounce, A. A. Quantum Instrumentation Control Kit – Defect Arbitrary Waveform Generator (QICK-DAWG): A Quantum Sensing Control Framework for Quantum Defects. 2023; `https://arxiv.org/abs/2311.18253`.

(2) Whitefield, B.; Toth, M.; Aharonovich, I.; Tetienne, J.-P.; Kianinia, M. Magnetic Field Sensitivity Optimization of Negatively Charged Boron Vacancy Defects in hBN. *Advanced Quantum Technologies* **2024**, 2300118.

(3) Dréau, A.; Lesik, M.; Rondin, L.; Spinicelli, P.; Arcizet, O.; Roch, J.-F.; Jacques, V.

Avoiding power broadening in optically detected magnetic resonance of single NV defects for enhanced dc magnetic field sensitivity. *Phys. Rev. B* **2011**, *84*, 195204.

(4) Gottscholl, A.; others Initialization and read-out of intrinsic spin defects in a van der Waals crystal at room temperature. *Nature Materials* **2020**, *19*, 540–545.

(5) Yu, P.; others Excited-State Spectroscopy of Spin Defects in Hexagonal Boron Nitride. *Nano Letters* **2022**, *22*, 3545–3549.

(6) Mu, Z.; others Excited-State Optically Detected Magnetic Resonance of Spin Defects in Hexagonal Boron Nitride. *Physical Review Letters* **2022**, *128*, 216402.

(7) Mathur, N.; others Excited-state spin-resonance spectroscopy of V_B^- defect centers in hexagonal boron nitride. *Nature Communications* **2022**, *13*, 3233.

(8) Gao, X.; others High-Contrast Plasmonic-Enhanced Shallow Spin Defects in Hexagonal Boron Nitride for Quantum Sensing. *Nano Letters* **2021**, *21*, 7708–7714.

(9) Xu, X. et al. Greatly Enhanced Emission from Spin Defects in Hexagonal Boron Nitride Enabled by a Low-Loss Plasmonic Nanocavity. *Nano Letters* **2023**, *23*, 25–33, PMID: 36383034.